FI SEVIER

Contents lists available at ScienceDirect

Corrosion Science

journal homepage: www.elsevier.com/locate/corsci



Near-infrared light controlled fast self-healing protective coating on magnesium alloy



Lei Huang^a, Jun Li^b, Wei Yuan^c, Xiangmei Liu^{a,**}, Zhaoyang Li^b, Yufeng Zheng^{c,**}, Yanqin Liang^b, Shengli Zhu^b, Zhenduo Cui^b, Xianjin Yang^b, Kelvin Wai Kwok Yeung^d, Shuilin Wu^{a,b},

- ^a Ministry-of-Education Key Laboratory for the Green Preparation and Application of Functional Materials, Hubei Key Laboratory of Polymer Materials, School of Materials Science & Engineering, Hubei University, Wuhan. China
- b School of Materials Science & Engineering, the Key Laboratory of Advanced Ceramics and Machining Technology by the Ministry of Education of China, Tianjin University, Tianjin 300072, China
- ^c State Key Laboratory for Turbulence and Complex System and Department of Materials Science and Engineering, College of Engineering, Peking University, Beijing 100871, China

ARTICLE INFO

Keywords: Magnesium alloy Degradation Photothermal Self-healing Light-controlled

ABSTRACT

We designed a photo-controlled degradative coating of polypyrrole (PPy)/ polycaprolactone (PCL) hybrids on biodegradable MgSr alloy. The photothermal effects of PPy inspired by near-infrared light (NIR) irradiation (808 nm) can locally heat the coating to the low melting-point temperature required for PCL within 6 min, which can quickly heal the scratched defects and contribute to control the degradation behaviors of magnesium alloy. The scratched region can get desired recovery of its corrosion resistance after NIR irradiation, as a result of the synergistic function of low-melting-point deformation of the coating matrix and photothermal effect of PPy.

1. Introduction

As having the great superiority of light-weight, large modulus of elasticity, high electrical conductivity and ect, magnesium-based alloys have substantial applications in the industries of medical apparatus, automotive and aerospace [1–3]. However, it is the redox reaction started by the existence of galvanic cell at the surface of Mg alloy that induces fast corrosion rate and thus severely restricts the wide development, application and dissemination of magnesium alloys [4–6]. Considering that the great necessity of endowing and keeping anticorrosive or other functional characteristics of magnesium alloys in the service life, it is widely accepted to develop a self-healing coating that can exert stimuli-responsive behavior and heal rapidly at the attacked area in corrosive environment [7–9].

Recently, increasing interests exist in the exploitation of smart polymer coatings, such as self-healing coatings, which can repair the attack and damage areas by themselves with minimal or no external stimulus [10–12]. There are two main categories of self-healing mechanism, including autonomous and non-autonomous methods. The early studied mechanism of autonomous self-healing is through

releasing corrosion inhibitors to achieve in-situ recovering at the defects [13]. However, the corrosion inhibitors such as hexavalent chromium [14], 8-hydroxyquinoline (8HQ) [15], and benzotriazole (BTA) [16], are not suggested to put into application practically, due to the hidden danger of the existence of human carcinogen and environmental pollution [17]. Non-autonomous self-healing is often carried out through responsive behavior to external stimulus, for instance, electric field [18], ultraviolet light [19], ionic strength [20], voltage [21], pH [22,23], or a combination of them. Sensitive response to multi-stimuli and high healing efficiencies make non-autonomous self-healing systems play an important role in corrosion protection. External stimulus can serve as an accurate and remote actuation switch to provide another promising solution to meet multi-field application and multi-purpose requirements.

Light can be a prior choice among all external stimuli sources. Ultraviolet (UV) radiation tends to result in destruction of the conformation and microstructure of polymers. The more serious is that human skin probably suffers ray harm, resulting in increased skin cancer incidence due to long-time exposure to UV [24]. Considering that penetrability and non-invasiveness, near-infrared (NIR) light has

E-mail addresses: liuxiangmei1978@163.com (X. Liu), yfzheng@pku.edu.cn (Y. Zheng), shuilin.wu@gmail.com, shuilinwu@tju.edu.cn (S. Wu).

d Department of Orthopaedics& Traumatology, Li Ka Shing Faculty of Medicine, The University of Hong Kong, Pokfulam, Hong Kong, China

^{*}Corresponding author at: Ministry-of-Education Key Laboratory for the Green Preparation and Application of Functional Materials, Hubei Key Laboratory of Polymer Materials, School of Materials Science & Engineering, Hubei University, Wuhan, China.

^{**} Corresponding authors

been employed in self-healing coating [17], photothermal therapy [25], or other light-induced controllable systems. Poly(ϵ -caprolactone) (PCL) has a low melt-point temperature about 60 °C [26]. NIR-irradiation-induced shape deformation of PCL can help to repair the damaged area due to molecular chain movement with a more timely and efficient fashion. Polypyrrole (PPy) could absorb near-infrared (NIR) light and convert it into thermal energy with a tunable temperature [27,28], which can in turn provide enough heat available for the changes of physical configurations in polymer networks [29]. Up to now, few studies reported the strategy of NIR-induced self-healing for aluminum alloy [17], silicon wafers [23], and carbon steel [19]. To our best knowledge, there are no research about this attempt or implement at magnesium alloys.

In this work, we hypothesize that the NIR-responsive polymer coating on magnesium alloys has the self-healing capacity triggered by photothermal method. The photothermal layer of PPy provides enough heat under short NIR irradiation to support the PCL layer to restore the corrosion damage on the surface. The collaborative effect developed from PCL/PPy composite polymer coating, can not only bring obvious improvement of stability in mechanical and chemical property, but also can help to design a low-toxicity or nontoxic self-healing coating. The composite polymer coating can achieve both keys of high photothermal efficiency and self-healing ability within a short time, assisting to build a multi-functional coating, which are also satisfied for practical and long-term requirement of repeated healing behavior with small loss in efficiency to avoid single use. Fig. 1 can clearly clarify the fabrication procedures and correlative self-healing mechanism. We expect this active platform to provide a remote and nondestructive control of fast self-healing and to offer long-term protection against corrosion.

2. Experimental procedures

2.1. Materials preparation and hydrofluoric acid (HF) treatment

Commercial Mg-1Sr alloys with dimensions of $\Phi 10 \times 5$ mm were served as targeted alloy materials. 2400-grit SiC papers were used to polish MgSr alloys. The obtained alloys were rinsed by ultrasonic cleaning in acetone and ethanol, at the last dried in air. The ground Mg-Sr alloy samples were immersed in hydrofluoric acid (HF, 40 wt%) for 24 h, then washed by distilled water for five times, finally dried in air.

2.2. Spin coating and PPy polymerization

The PCL particles ($M_w = 80,000$) was dissolved in dichloromethane with the concentration of 8% (w/v). By the spin coater (KW-4A), the spin process was carried out as follows. After the addition of 200 mL of PCL solution onto the surface of the PPy deposited samples, the samples were rotated at 600 rpm for 10 s, followed by a high rotating speed of 2000 rpm for 30 s. This process needed to be executed for three times at room temperature. The collected samples were called as F-PCL samples. Fe(NO₃)₃·9H₂O was used as an oxidant and the polymerization reactions were carried out in distilled water. First, Mg alloy samples were soaked in 10 mL distilled water, containing 114 mg of pyrrole (7.2 mmol). After the dissolution of Fe(NO₃)₃·9H₂O (0.4 g, 0.99 mmol) in 10 mL distilled water, and this obtained solution was added to the above pyrrole solution. The reaction needed to proceed for 2 h at 4 °C, and then the samples were washed 3 times in distilled water and dried in air. The F-PCL/PPy/PCL samples were obtained by conducting PCL spinning process on the F-PCL/PPy samples for ten times, with the same spinning process as above.

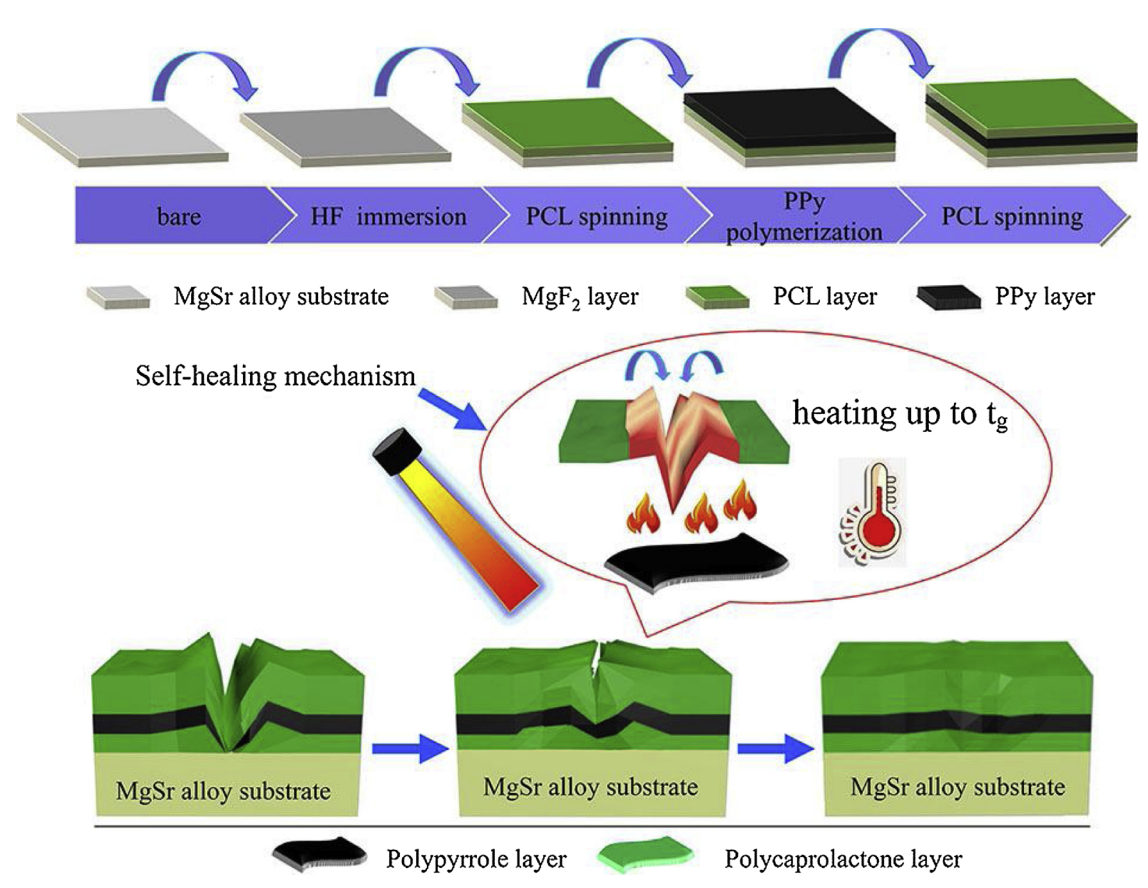


Fig. 1. Fabrication and self-healing process of PCL/PPy composite polymer coating on MgSr alloy substrate with the assistance of NIR light.

2.3. Surface characterization

SEM (JSM6510LV) was applied to observe coatings' morphologies and cross-section. The presences of PCL and PPy were verified by FTIR (Nicolet IS10, USA). Differential Scanning Calorimetry (DSC-60) was utilized to detect the melt-point temperature of different samples. The absorbance at UV–vis spectroscopic spectra was determined by utilizing an UV–vis spectrophotometer (UV-3600, Japan).

2.4. Electrochemical corrosion measurements

The electrochemical workstation (CHI660E) was used to measure and evaluate the corrosion performances of MgSr samples in simulated body fluid (SBF, pH = 7.4) and also at set temperature of 37 °C. The standard three-electrode cell used in this tests was installed. Taken all electrochemical tests at a stable open circuit potential (OCP) was required. A sinusoidal potential of 10 mV was set for electrochemical impedance spectroscopy (EIS) with the scanning rate of 2 mV·s $^{-1}$, in a range of 10^5 Hz to 10^{-2} Hz. The scanning rate of the potentiodynamic polarization test was set as $2\,\text{mV·s}^{-1}$. Each test was repeated for three times and results was analyzed by the software Zsimpwin 3.21.

2.5. pH evolution and Mg release behavior

The 14-day continuous immersion tests in SBF maintained at 37 $^{\circ}$ C, and the ratio of the SBF volume to different samples weight is 30:1. The pH values and leaching content of Mg ions were monitored. Each sample was measured at 13 time points, 0, 2, 4, 8, 12 and 24 h on the first day, and then 3, 5, 7, 9, 11, 13, and 14 days. The ICP-AES (Opitmal 8000) was used to detect the released content of Mg²⁺, with the concentration diluted to 20%. Afterward, all specimens were rinsed in distilled water and dried.

2.6. Self-healing testing

Scratch tests were performed by using a automatic scratch tester to make a through-coating scratch on the surface. The blade was plunged into the surface at a constant force of 15 N. The scratches were deep enough to penetrate the coatings and reached the AZ31 Mg alloy substrate. The surface of the Mg alloy was likely to be scratched during scratch treatmeat, due to the softness of Mg alloys. To get a comprehensive view about the principle of coating's self-healing process, the unrepaired coating was under NIR light irradiation for 6 min to realize the shape deformation behavior of the F-PCL/PPy/PCL coating. The temperature change and heat maps were recorded by the IR thermal imager (testo 875i, Testo Instruments International Trading, Shanghai Co., Ltd) every 30 s. The repaired morphology was detected by SEM.

2.7. Scanning vibrating electrode technique (SVET) measurements

SVET measurements were conducted on an M370 scanning electrochemical workstation (Ametek, USA) to detect the real-time current density of the AZ31 Mg alloy surface. All samples were fixed to an epoxy resin holder and immersed in 0.05 M NaCl solution. A Pt-Ir microprobe was served as the vibrating microelectrode equipped with a Pt black tip (15 μm in diameter), which kept the vertical distance of 100 μm over the tested surface. The scans were seted to start after 40 min immersion, and the peak-to-peak amplitude was 30 μm . The electric current densities were displayed by 3D maps.

3. Results and discussion

3.1. Synthesis and characterizations

As shown in Fig. 2a, the bare samples' surface was flat, but there were several holes spread on the surface after hydrofluoric acid (HF)

treatment (Fig. 2b). The pretreatment was to prepare a MgF2 layer acted as a barrier with weaker protection against corrosion [30,31]. The F-PCL samples were prepared by spinning three layers of PCL on the MgF2 samples. The F-PCL/PPy were obtained by in-situ oxidative polymerization of PPy on the surface of F-PCL samples [32,33]. In order to achieve ultrafast self-healing behavior, ten layers of PCL were spinned on the substrate of F-PCL/PPy samples, which were named as F-PCL/PPy/PCL. The surface of F-PCL/PPy/PCL was smooth and flat as presented in Fig. 2c. The width of the scratch was about 10 µm before NIR irradiation (in Fig. 2d) and seemed completely repaired after NIR irradiation (in Fig. 2e), with the protuberance around the scratch. The F-PCL samples possessed a coating thickness of about 30 µm (in Fig. 2f). After PPv polymerization, the surface morphology of F-PCL/PPv was irregular with an approximate thickness of 40 µm (in Fig. 2g). The depth of section about F-PCL/PPy/PCL is near 160 µm in Fig. 2h. After scratch treatment, Figure S1 showed there still remained the scratch on the metallic surface after remove of the coating.

FT-IR analysis of the freshly prepared F-PCL/PPy film confirmed the presence of PPy. As shown in **Figure S1**, PPy peaks were located at around 1550 cm⁻¹, while the peak at 1200 cm⁻¹ belonged to C=C/C-C stretching. As for the two peaks at 1370 and 1030 cm⁻¹, the former should be assigned to C=N stretching while the latter is originated from the plane bending vibrations of C=H bonding [34]. The PPy peaks can no longer be observed after followed spinning layer of PCL. The PCL films were confirmed by the appearance of specific spectrum peaks, which were located at 2944 cm⁻¹, 1720 cm⁻¹, and 1240 cm⁻¹, assigned to asymmetric stretching of CH2, C=O stretching and asymmetric stretching of C=O=C [35]. The results of UV-vis spectra were shown in Fig. 3a, as for the F-PCL/PPy film, there was obvious absorption in near infrared region. After spinning PCL layer for ten times, the absorption became weaker, but was still higher than the F-PCL film.

3.2. DSC assay

Herein, if the surface temperature rises over the glass transition temperature (T_g), the scratched area on samples' coating can be remedied by NIR irradiation. DSC curves (in Fig. 3b) revealed that the obvious endothermic peaks of the pure PCL layer and PCL/PPy/PCL were about 59.5 °C and 62.2 °C. PPy was in stable state at low temperature and served as the middle layer in sandwich-like structure, and PPy exerted little impact on the Tg of PCL. This result also indicated a certain compatibility between the two functional layer of PPy and PCL. Based on the DSC results, the self-healing actions triggered by shape deformation were expected to be performed on the scratched surface of the coatings. NIR irradiation relaxed the restrictions on the movement of polymer chain segment, and PCL were expected to melt and flow into the scratched area to restore integrity as much as possible, together with the PPy layer. Polycaprolactone and polypyrrole were relatively stable near the T_g of PCL. Under NIR irradiation, polypyrrole still kept solid state, polycaprolactone had a tendency to flow. The two substances cannot dissolve into each other, and the interlayer of PPy will keep pace with the PCL layer's movements.

3.3. Photothermal effect

Upon exposure to an 808-nm NIR laser (0.585 W/cm²), an IR thermal imager was used to detect the heating behavior of bare and F-PCL/PPy/PCL coated MgSr alloys. The bare MgSr was set as the control and the two groups were performed under solvent-free condition. The temperature profiles are shown in Fig. 3c, which was recorded every 30 s, and the cyclic irradiation curves are shown in Fig. 3d. Under NIR irradiation, the temperature of the F-PCL/PPy/PCL coated samples increased rapidly and reached a turning point about 62.5 °C within 4 min, followed with a relatively stable platform in the remaining 2 min. In comparison, the temperatures of the bare samples only increased by roughly 1 °C.

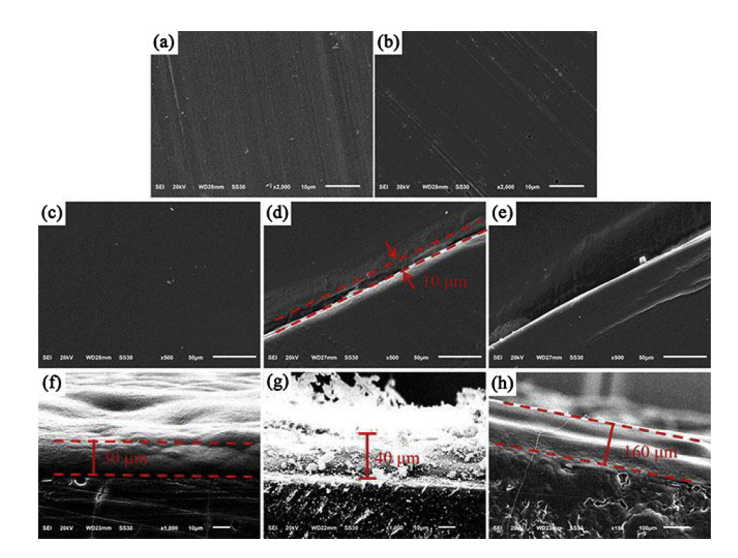


Fig. 2. Surface characterizations of different MgSr alloys samples: the morphology of (a) bare samples, (b) MgF₂ samples, (c) the F-PCL/PPy/PCL samples, (d) the scratched F-PCL/PPy/PCL samples, (e) the healed F-PCL/PPy/PCL samples; (f), (g) and (h) corresponding to the cross-sectional image of the F-PCL samples, the F-PCL/PPy samples and the F-PCL/PPy/PCL samples.

The heat maps of the F-PCL/PPy/PCL coating are shown in Fig. 3e, revealed that temperature difference between points distributed on the round surface varied little, with a maximum temperature of about

64.1 °C. The homogeneous temperature field on the whole surface indicated that PPy particles were evenly deposited on the surface of MgSr alloys. In addition, a high level of transparency afforded by PCL film

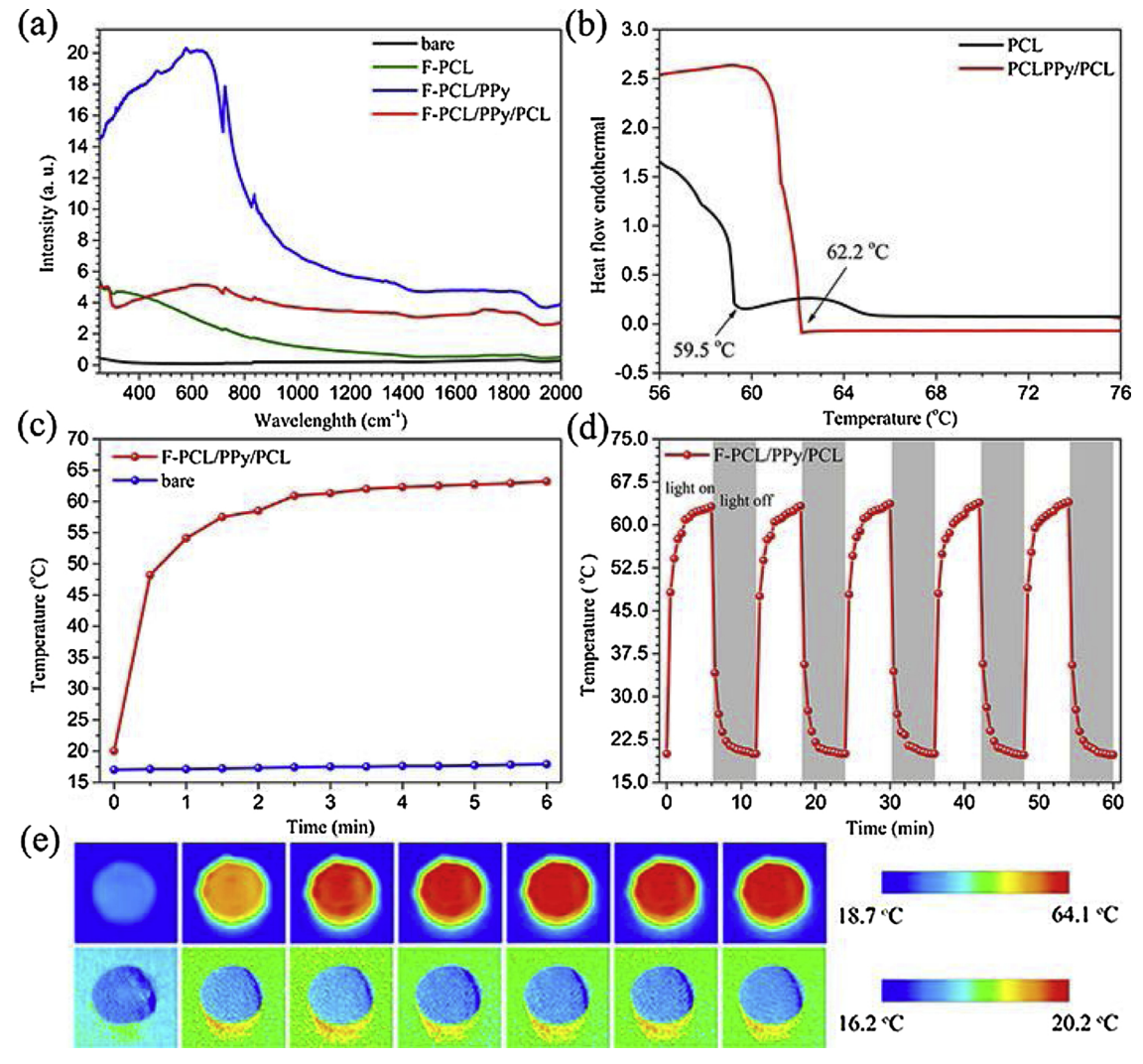


Fig. 3. (a) UV-vis-NIR absorption of the bare, F-PCL, F-PCL/PPy and F-PCL/PPy/PCL samples; (b) DSC of the PCL and PCL/PPy/PCL films (c) The temperature changes of the bare and F-PCL/PPy/PCL samples under NIR irradiation; (d) Cyclic irradiation curves and corresponding (e) Infrared thermography of the bare and F-PCL/PPy/PCL samples.

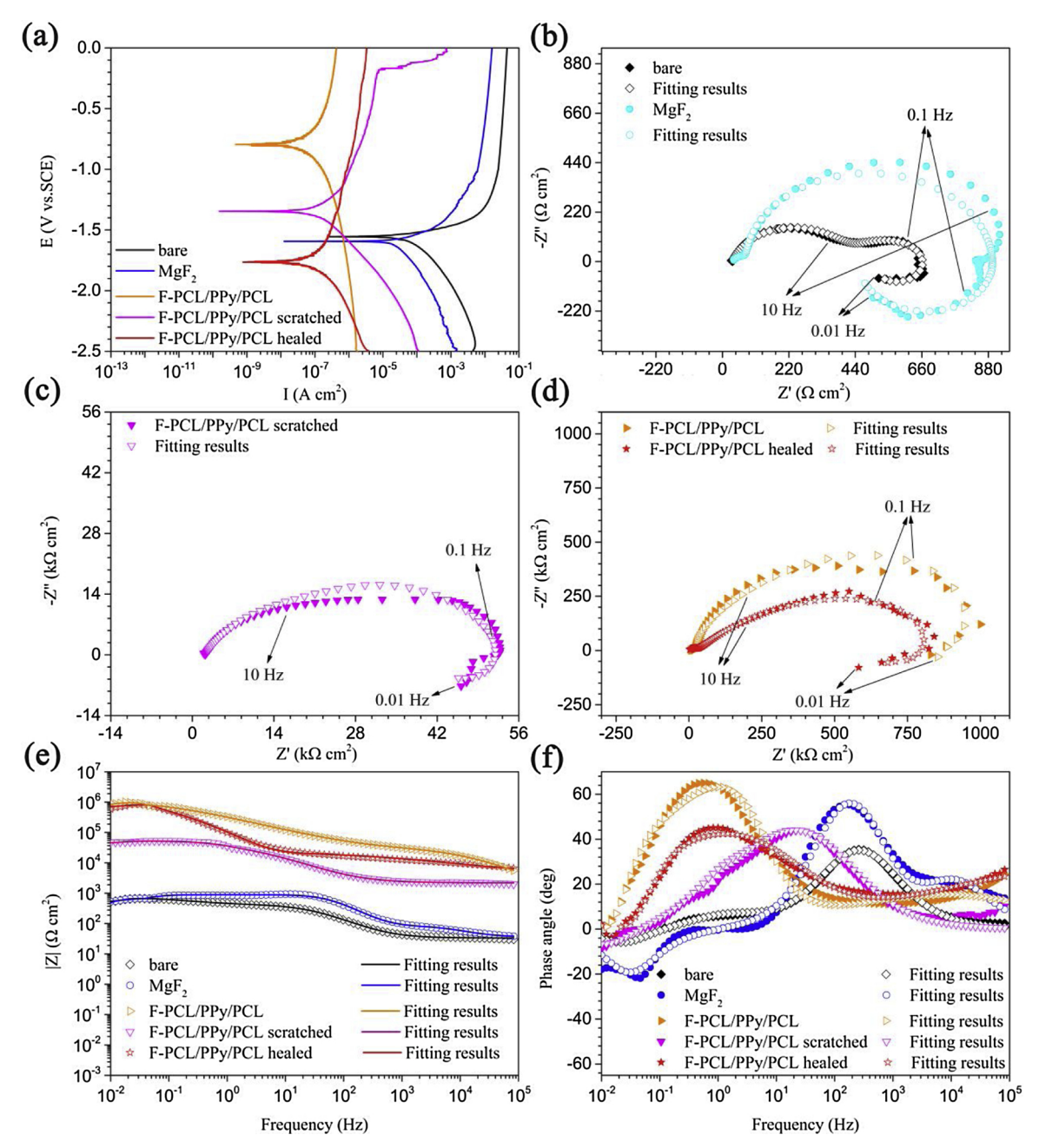


Fig. 4. Electrochemical tests of MgSr alloy samples after preparation procedures; (a) potentiodynamic polarization tests in SBF; (b), (c) and (d) Nyquist plots; (e) the module plots of impedance and (d) the phase plots of impedance.

was beneficial for deeper penetration of NIR light. The temperature of the bare metal surface was slightly lower than the ambient temperature at the beginning, temperature changed little after NIR treatment compared with distinct and rapid photothermal behavior of F-PCL/PPy/PCL. The above analytical results suggested that the PPy interlayered structure could play an on-demand role for exerting as an efficient photothermal agent, and most importantly, the heat generated from the composite coating was sufficient to trigger shape deformation afforded by PCL, as discussed in following sections.

3.4. Electrochemical measurements

To figure out the short-term and long-term corrosion evolution of different modified coatings, electrochemical measurements were taken to explore the barrier properties and self-healing properties after 0, 1, 3, 5 and 7 days of immersion. Corrosion density deduced from Tafel

curves can reflect the corrosion resistance and help to judge whether the corrosion resistance gets recovery or not [36,37]. In Fig. 4a, the corrosion current density deduced from Tafel extrapolation followed the order: F-PCL/PPy/PCL < F-PCL/PPy/PCL healed < F-PCL/PPy/PCL scratched < MgF $_2$ < bare. It is generally recognized that a material has more negative E_{corr} , the less noble it is. In Fig. 4a, the bare AZ31 alloy had more positive E_{corr} values but less corrosion resistance than the healed F-PCL/PPy/PCL samples according to the EIS test. In fact, the E_{corr} is a thermodynamic characteristic of a given metal-electrolyte system, not directly reflecting the kinetics of material corrosion [38,39]. Based on the analysis of the corrosion process, we may ascribe this result to the co-occurrence of Mg dissolution through the pores or defects, formation of the corrosion product layer and increase in interfacial pH, which caused E_{corr} values fluctuate.

Fig. 4 exhibits the consequences of electrochemical impedance spectroscopy (EIS), including Nyquist plot (Fig. 4b, c and d), module

plots of impedance (Fig. 4e), phase plots of impedance (Fig. 4f) and fitting curves. Three characteristic loops existed in EIS results. The capacitive loops at the high and middle frequency were as results of charge transfer and mass transport, the inductive loop at the low frequency was related to pitting corrosion on the intersurface between Mg alloy and the electrolyte solution [6]. The $|Z|_{0.01Hz}$ in Bode diagram represented the impedance modulus at 0.01 Hz, and the dimension of capacitive loop in Nyquist plots and $|Z|_{0.01 Hz}$ have been deemed as credible indicators for analyzing and comparing the corrosion resistance of different coatings. The larger capacitive loop and the higher of $|Z|_{0.01 Hz}$ value indicated better protective capacity against corrosion. In Fig. 4e, the $|Z|_{0.01 Hz}$ value can be expressed as the following trend: bare < MgF₂ < F-PCL/PPy/ PCL scratched < F-PCL/PPv/PCL healed < F-PCL/PPv/PCL. The healed F-PCL/PPy/PCL coating restored about 76.7% of |Z|_{0.01Hz} value after NIR irradiation. However, the scratched F-PCL/PPy/PCL coating could only remain approximately 5% of the $|Z|_{0.01Hz}$, due to the fact that the exposed surface at the scratch region damaged the integrity and the compact of the coating. As a result of these effects, diffusion passways were easily opened and local corrosion were also accelerated. In the lowfrequency region (typically in range of $0.1 \sim 0.01$ Hz), the phase angle (in Fig. 4f) reflected pitting corrosion at the interface [40,41]. The phase angle of the F-PCL/PPy/PCL and the healed F-PCL/PPy/PCL coating in the low-frequency region were higher than that of the scratched F-PCL/ PPy/PCL, MgF2 and bare samples, due to the decreased dimension of

Generally, the high-frequency loop of untreated Mg alloy represents the formation of oxides or hydroxides at the interface. Herein, low frequency inductive loop was obvious in bare AZ31 and MgF $_2$ samples, indicating the occurrence of pitting corrosion. However, the F-PCL/PPy/PCL, the scratched F-PCL/PPy/PCL and the healed F-PCL/PPy/PCL samples, showed capacitive loops at most frequencies with weak inductive regions in the low frequencies. Cracked and porous coatings could not afford effective protection, but compact coatings can delay the pitting corrosion, thus hindering the charge transfer process at interfaces and weakening of the inductive loops. Therefore, coatings with better barrier properties showed increased phase angle in the low-frequency region, as shown in phase angle ν s. log f curves (Fig. 4f).

With the immersion time increased to 1 day, the i_{corr} values were obviously increased (in Figure S3a) and the capacitive loops also fell into decline (in **Figure S3b**). The values of $|Z|_{0.01Hz}$ in the F-PCL/PPy/ PCL, the healed F-PCL/PPy/PCL and the scratched F-PCL/PPy/PCL coatings decreased from $9.3 \times 10^5 \ \Omega \ cm^2$ to $7.8 \times 10^5 \ \Omega \ cm^2$, $7.1\times10^5\,\Omega$ cm² to $2.8\times10^5\,\Omega$ cm² and $4.7\times10^4\,\Omega$ cm² to 8.1×10^3 Ω cm² (in Figure S3c). The time constant at low frequency (10⁻² $Hz \sim 10^0$ Hz) observed in **Figure S3d**, suggested that the electrolyte had reacted with the substrate and the appearance of corrosion [42]. After 3 days, the electrolyte ions penetrated the coating matrix, resulting in a continuous increase in i_{corr} (in Figure S4a) and decreased capacitive loops (in Figure S4b). The values of $|Z|_{0.01 \mathrm{Hz}}$ (in Figure S4c) in the F-PCL/PPy/PCL, the healed F-PCL/PPy/PCL and the scratched F-PCL/ PPy/PCL coatings decreased to $4.3 \times 10^5~\Omega~cm^2, 1.5 \times 10^5~\Omega~cm^2$ and $5.3 \times 10^3 \,\Omega$ cm². In **Figure S4d**, the high frequency impedance did not shift with the immersion time increased, but overlapped each other.

As immersion time continued to 5 days, the i_{corr} (in **Figure S5a**) further rose to 2.514×10^{-6} A cm², 1.984×10^{-5} A cm² and 1.003×10^{-5} A cm² in the F-PCL/PPy/PCL, the scratched F-PCL/PPy/PCL and the healed F-PCL/PPy/PCL coatings, with smaller capacitive loops (in **Figure S5b**). Correspondingly, the $|Z|_{0.01Hz}$ values (in **Figure S5c**) decreased to $1.7 \times 10^5 \,\Omega$ cm², $5.3 \times 10^4 \,\Omega$ cm² and $3.3 \times 10^3 \,\Omega$ cm², respectively. Phase angle in the medium-frequency region was associative with the coating's pore resistance and oxidation film on the exposed surface [43]. The time constant observed at medium frequency ($10^0 \,\text{Hz}$ – $10^3 \,\text{Hz}$) in **Figure S5d**, indicated the formation of corrosion product layer to inhibit the continued corrosion activities between electrolyte and substrate [44]. After 7 days, the upward trend in the i_{corr} (in Fig. 5a) further rose to $7.253 \times 10^{-6} \,\text{A cm}^2$, $4.505 \times 10^{-5} \,\text{A cm}^2$ and

1.584 × 10⁻⁵ A cm² in the F-PCL/PPy/PCL, the scratched F-PCL/PPy/PCL and the healed F-PCL/PPy/PCL coatings, still in cooperation with smaller capacitive loops (in Fig. 5b). The values of $|Z|_{0.01Hz}$ in the F-PCL/PPy/PCL, the healed F-PCL/PPy/PCL and the scratched F-PCL/PPy/PCL coatings dropped to $2.2 \times 10^4 \ \Omega \ cm^2$, $1.7 \times 10^4 \ \Omega \ cm^2$ and $2.2 \times 10^3 \ \Omega \ cm^2$, respectively (in Fig. 5c). The time constant was still observed at medium frequency (10⁰ Hz–10³ Hz) in Fig. 5d, indicating that the F-PCL/PPy/PCL, the healed F-PCL/PPy/PCL and the scratched F-PCL/PPy/PCL coatings can still keep the coatings' barrier property.

The EC1 of R(C(R(CR(RL)))) and EC2 of R(O(R(OR(RL)))) could be utilized as suitable equivalent circuit (EC) models. The fitting parameters of equivalent circuit are respectively presented in Fig. 6 and **Table S1. 2. 3. 4 and 5.** The EC1 was well fit for bare Mg and MgF₂ samples, and the EC2 was credible for the F-PCL/PPy/PCL, the healed F-PCL/PPy/PCL and the scratched F-PCL/PPy/PCL samples. With regard to impedance parameters, the standard deviation was controlled within the order of $1 \times 10^{-3} \sim 1 \times 10^{-4}$. In these equivalent, R_s represented the solution resistance, R₁ was the charge transfer resistance, also represented the resistance to the electron transfer of the faradic process on AZ31 Mg alloy, in parallel with the double layer capacitance C₁ [45,46]. A constant phase element Q₁ in the EC2 was used to instead C₁ for the F-PCL/PPy/PCL, the healed F-PCL/PPy/PCL and the scratched F-PCL/PPy/PCL samples, due to the fact that Nyquist plots of these samples showed depressed semicircles [47]. An ideal capacitor C2 and a resistance R2 were proposed to account for the capacitance and resistance of the corrosion product layer formed on the surface of Mg alloy. In the EC2, C2 was exchanged for constant phase element Q2 to better fit the EIS results. An inductance (L) and a resistance $(R_{L)}$ were introduced to explain the inductive behavior. The value of $|Z|_{0.01Hz}$ (in **Figure S5a**) as well as the R_2 (in **Figure S5b**) can be viewed as crucial indicators, reflecting the barrier property and degradation property of the protective coating. As immersion time continued, the R_2 and $|Z|_{0.01Hz}$ of the three kinds of coating were together in a downward trend. The healed F-PCL/PPy/PCL coating could not recover the same intact as before and there were still some small defects in coating allowing permeation of electrolyte. From the damage evolution of the two indicators, the degradation rate of the protective coating was dependent upon the sealing levels of scratch.

The change in R_2 and $|Z|_{0.01Hz}$ measured as a function of immersion time revealed the corrosion process of AZ31 Mg alloy, as well as the R₁ and Q₁ used for the reflecting indicators. During immersion time of 72 h, a steady decrease in R₁ and a increase in O₁ in the scratched F-PCL/PPy/PCL indicated the thickness of protect coating reduced and corrosion process accelerated. The same phenomenon happened in the healed F-PCL/PPy/PCL during 24 h and 72 h-120 h immersion, as well as in the F-PCL/PPy/PCL samples during 120 h-168 h immersion. It can also be observed some fluctuations in R₁ and Q₁ during the whole immersion. For the compact F-PCL/PPy/PCL samples, R1 increased a bit and Q₁ decreased slightly during 1-day immersion. This is due to the formation of insoluble corrosion products on the surface, hindering the charge transfer process. Immersion time between 24-72 h, the healed F-PCL/PPy/PCL showed the downtrend in R₁ and uptrend in Q₁, due to the same reason as above. The variations in R₁ and Q₁ can also help us analyse the corrosion behavior of AZ31 Mg alloy.

Fig. 7 presents the surface morphologies of different MgSr alloy samples after three- or seven-day immersion and followed electrochemical tests. The surface of intact F-PCL/PPy/PCL coating still remained compact and some species from the electrolyte solution tended to be absorbed onto the substrate after three-day immersion (Fig. 7a). However, the outer layer of PCL film was inclined to degrade after seven-day immersion in Fig. 7b. There were some holes spread on the scratched F-PCL/PPy/PCL coating after three-day immersion and the integrity of the film was damaged in Fig. 7c. Fig. 7d shows that the crack region suffered more severe corrosion after seven-day immersion. As for the healed F-PCL/PPy/PCL coating, although there was some unrepaired region, most of the surface remained compact and relatively

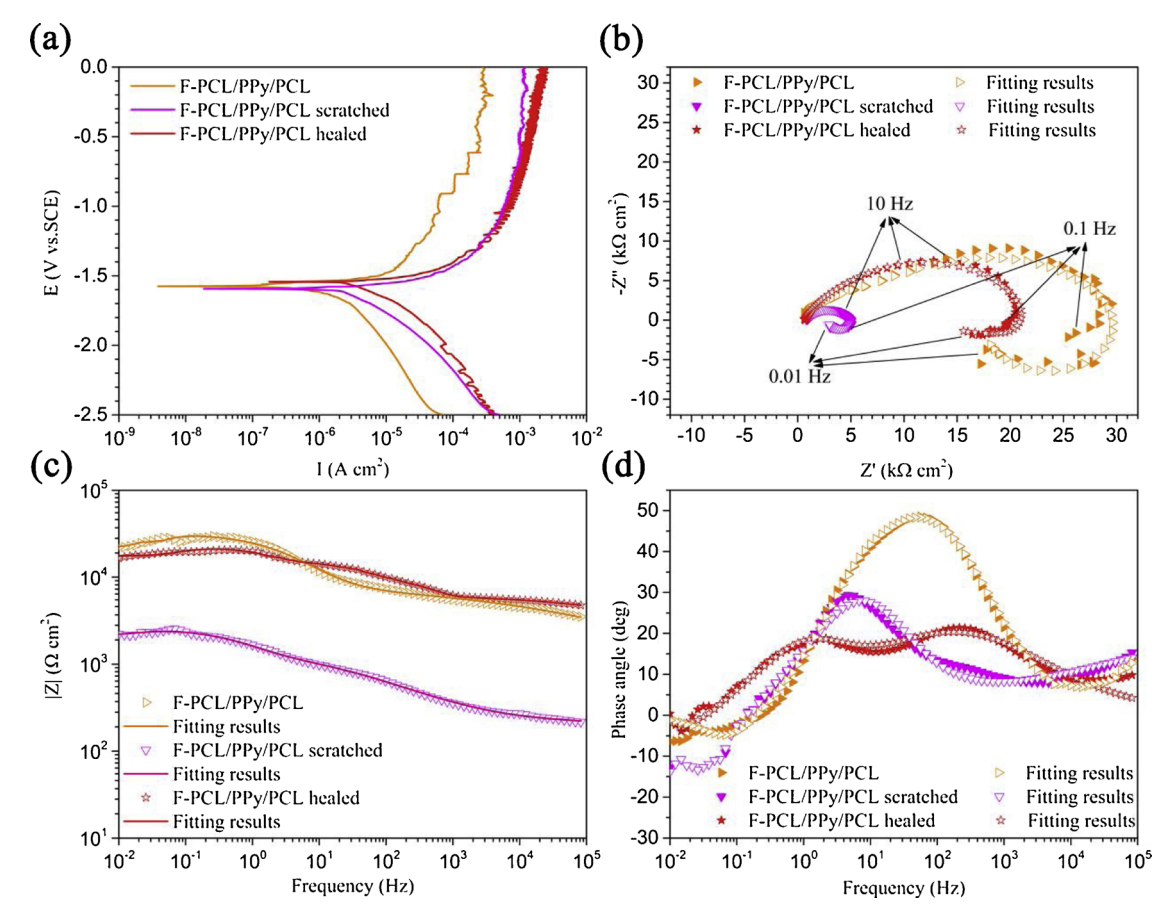


Fig. 5. Electrochemical tests of MgSr alloy samples after seven-day immersion; (a) potentiodynamic polarization tests; (b) Nyquist plots; (c) the module plots of impedance and (d) the phase plots of impedance.

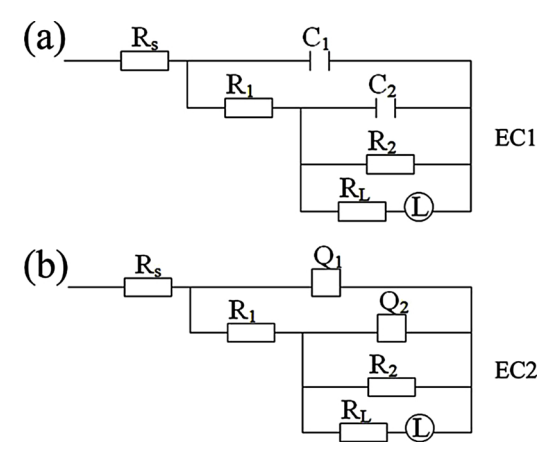


Fig. 6. The diagram of Equivalent circuits of EIS results: (a) EC1 for bare MgSr and MgF $_2$; and (b) EC2 for the intact, scratched and healed F-PCL/PPy/PCL samples.

smaller area tended to degrade after three-day immersion (in Fig. 7e). However, after seven-day immersion (in Fig. 7f), the unrepaired scratched region in the healed F-PCL/PPy/PCL film tended to suffer serious corrosion, as well as the outer surface.

3.5. Immersion tests

During immersion period, cathodic reaction induced hydrogen production and anodic dissolution were prone to happen on MgSr alloy's surface. MgSr alloys were susceptible to corrosion in the electrolyte containing corrosive ions. The release of Mg ions and the pH values

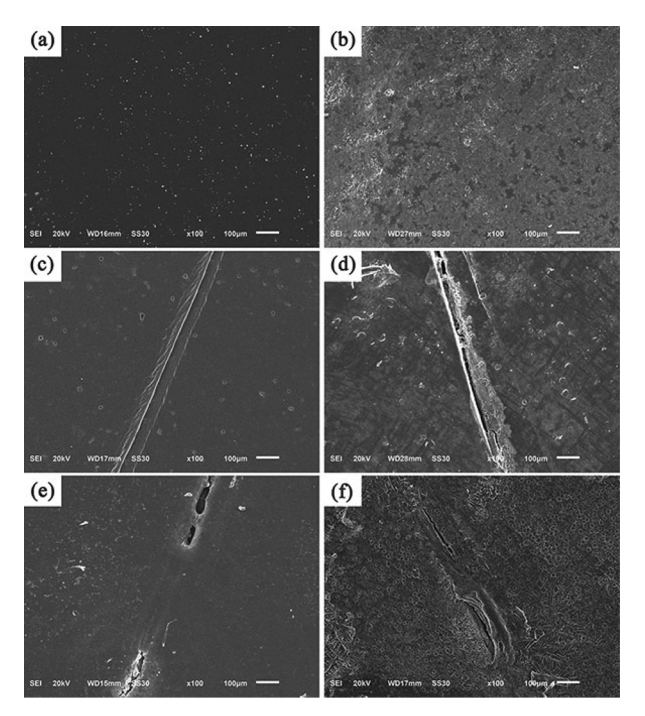


Fig. 7. Surface morphologies of different MgSr samples after different immersion periods and the followed electrochemical experiments: (a) and (b) corresponding to the F-PCL/PPy/PCL samples after three-day and seven-day immersion; (c) and (d) corresponding to the scratched F-PCL/PPy/PCL samples after three-day and seven-day immersion; (e) and (f) corresponding to the healed F-PCL/PPy/PCL samples after three-day and seven-day immersion.

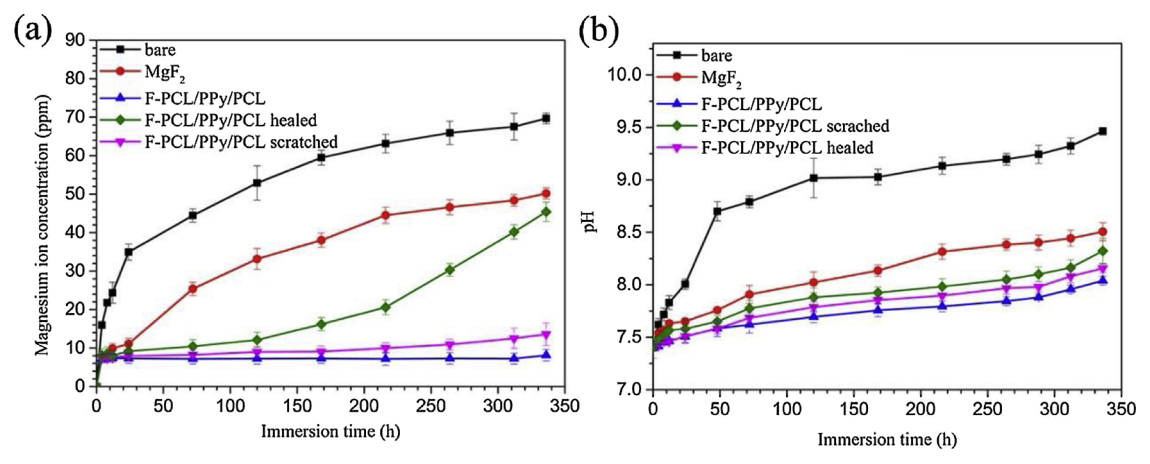


Fig. 8. Immersion tests in SBF: (a) the concentration of Mg^{2+} released from MgSr alloy samples during immersion time; (b) the evolution of pH values during immersion time. The experiments were executed for three times as well as under the same and independent condition (n = 3), and data were mean \pm SD.

were served as powerful auxiliary tools for qualitative and quantitative corrosion analysis. In Fig. 8a, while the immersion time increased from 4 to 336 h, the released concentration of the Mg ions increased from 15.96 ppm to 69.69 ppm with regard to bare samples. In contrast, an evident slowdown was observed in the concentrations of Mg ions from the modified samples over time, shown as 7.66 ppm to 50.18 ppm (MgF_2) , 7.23 ppm to 8.12 ppm (F-PCL/PPy/PCL), 8.13 ppm to 45.4 ppm (F-PCL/PPy/PCL scratched), 7.39 ppm to 13.08 ppm (F-PCL/PPy/PCL healed), respectively. The fluorinated surface by hydrofluoric acid etching could only provide limited protection under long-term immersion in electrolyte solution. After two-time spinning of PCL and deposition of PPv, the corrosion phenomena were under desired control over a long period of 14 days. With regard to the scratched F-PCL/PPy/ PCL samples, a rapid growth in the content of released Mg ions were shown in the later stages of immersion. The accelerated rate of releasing Mg ions was ascribed to the fact that the scratched areas were easy to be attacked by the corrosive ions such as Cl and so on. The healed samples showed a relatively lower rate of corrosion process, with about one-fifth of released Mg ions from the F-PCL/PPy/PCL samples with scratch treatment.

During immersion time from 4 h to 336 h, the pH evolution of different samples was shown in Fig. 8b as the following trend, 7.62 to 9.46 (bare), 7.54 to 8.6 (MgF₂), 7.41 to 8.04 (F-PCL/PPy/PCL), 7.42 to 8.16 (F-PCL/PPy/PCL healed), 7.47 to 8.33 (F-PCL/PPy/PCL scratched). These results were in consistent with the release of Mg ions. Much faster changes of pH were detected on the scratched F-PCL/PPy/PCL samples. MgF₂ coated samples showed slightly lower speed of pH change. There is not much difference between the F-PCL/PPy/PCL samples and the healed F-PCL/PPy/PCL samples in the term of pH change. The scratched F-PCL/PPy/PCL samples also showed an increasing rate of pH value. The existence of scratch exerted negative effect on corrosion resistance of the coating and did not benefit for long-term stage of corrosion protection.

3.6. Local corrosion behavior of AZ31 Mg alloy using SVET

SVET has been used extensively to examine the corrosion mechanism of Mg alloys [48,49]. The anodic current density peak $(i_{A,max})$ and the cathodic current density peak $(i_{C,max})$ from the current density map were used to characterize the coating's anti-corrosion properties [50]. The SVET maps of the scratched F-PCL/PPy/PCL and healed F-PCL/PPy/PCL presented in Fig. 9, with different distribution maps of current densities. Because of the scratch treatment, the anodic current density of the scratched F-PCL/PPy/PCL was higher than $80\,\mu A\,cm^{-2}$ and cathodic current densities lower than $-75\,\mu A\,cm^{-2}$, indicating the corrosion activities taken activly on the scratched area in early

immersion time, as shown in Fig. 9a. After NIR irradiation, The corrosion densities of the healed F-PCL/PPy/PCL decreased from 80/75 $\mu A\, cm^{-2}$ (anodic/cathodic) to about 6.2/-1.0 $\mu A\, cm^{-2}$, as shown in Fig. 9b. These results were consistent with the EIS plots. The scratched area with the appearance of a large and sharp area of anodic current density was likely to lost its barrier property, and corrosion process accelerated through those cracks and pores. Fig. 9c and d also shows obvious discrepancy between anodic and cathodic areas. In comparison, the barrier property of the scratched area improved a lot after NIR irradiation.

3.7. Self-healing mechanism of F-PCL/PPy/PCL coating

To get a comprehensive understanding about the self-healing mechanism, the F-PCL/PPv/PCL coating was scratched and then under NIR irradiation for 6 min. The coatings' self-healing performance was evaluated by EIS tests performed in SBF solution at 37 °C. The value of |Z|0.01Hz in the healed F-PCL/PPy/PCL coating disclosed desired restoration efficiency up to 76.7% at the beginning of immersion. In sharp contrast, the preservation efficiency of |Z|_{0.01Hz} in the scratched F-PCL/ PPy/PCL coating only remained 5%, thus resulting in earlier loss of reservation of corrosion resistance. The value of |Z|_{0.01Hz} in the F-PCL/ PPy/PCL coating was still well above $2 \times 10^4 \Omega$ cm² after seven-day immersion, which was about one order of magnitude higher and 1.4 times higher than that of the scratched F-PCL/PPy/PCL and the healed F-PCL/PPy/PCL coatings, respectively. In the following immersion tests, the changes of pH values and releasing content of Mg ions in the healed F-PCL/PPy/PCL coating were slower than that in the scratched PCL/PPy/PCL coating. The better preservation performance against corrosion could be attributed to the NIR-triggered self-healing behavior to close and seal the scratch region.

As shown in Fig. 1, once the NIR light is applied on the scratch region, the medium layer of PPy owned excellent photothermal conversion efficiency, so it can heat to the melting point required for PCL within short time, prompting the shape deformation of PCL to lead the closure of the scratch. In addition, the degree of healing can be adjusted by extending or shortening the irradiation time. With longer irradiation time, the scratch will be closed more thoroughly. As for scratched F-PCL/PPy/PCL coating, electrolyte ions will permeate into the coating though crack, pore defect or other channels to corrode metal surface. However, after NIR irradiation, the repaired region still keep three-layer architecture as before, and the self-healing behavior exhibits good reproducibility and stability.

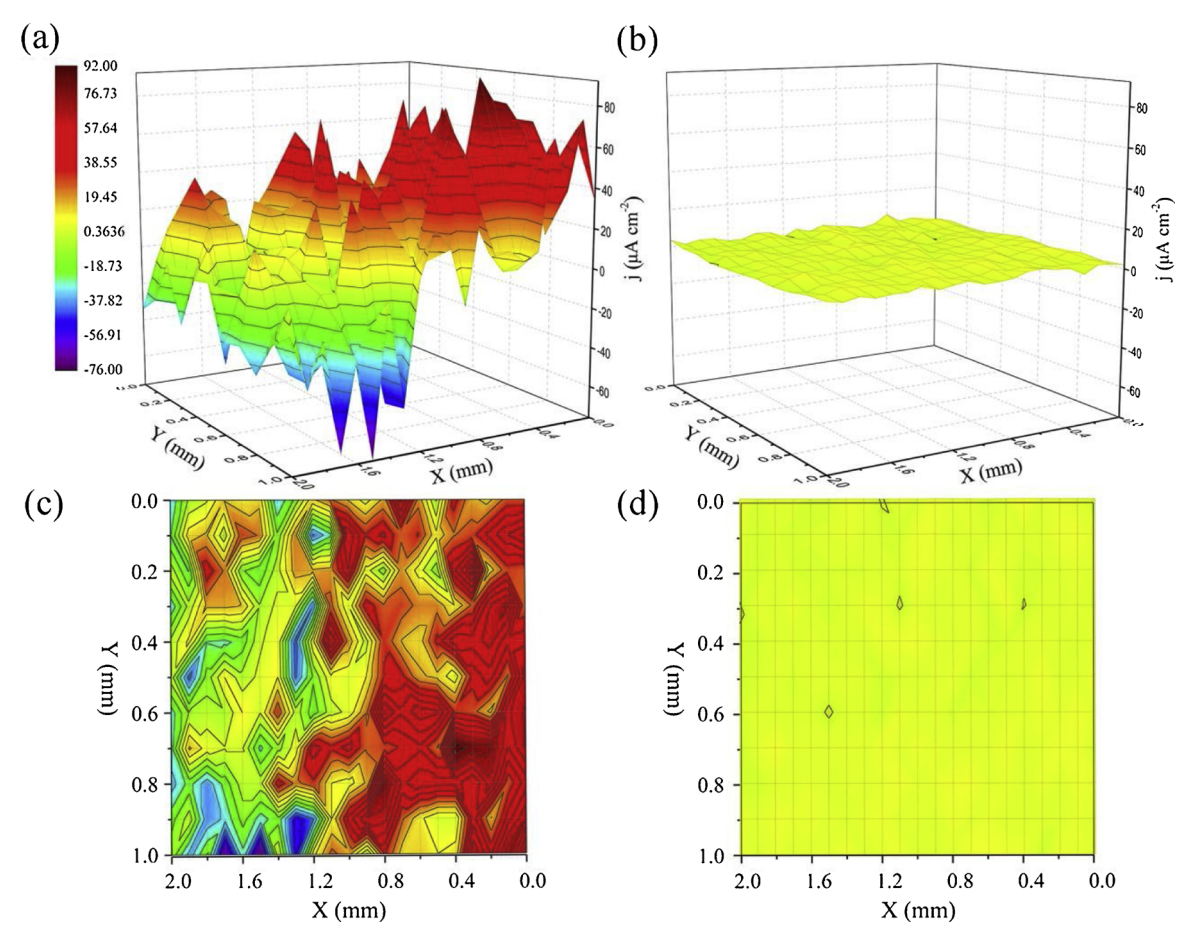


Fig. 9. SVET 3D maps of the electric current density measured above the surface of (a) the scratched F-PCL/PPy/PCL; (b) the healed F-PCL/PPy/PCL; (c) and (d) corresponding to the ichnography of (a) and (b).

4. Conclusion

In this work, a photo-controllable self-healing coating was designed to protect MgSr alloy from corrosion. The adoption of NIR laser treatment as an novel excitation and regulatory strategy can achieve better and fast recovery of self-healing performance. This goal was achieved by introducing the photothermal layer of PPy and the low-meltingpoint layer of PCL. The F-PCL/PPy/PCL hybrid coating demonstrated that the scratch region can be closed and sealed by the movement of polycaprolactone chain segment triggered by the shape deformation at the melt-point, which was under the great assistance of excellent photothermal conversion efficiency in PPy film. After NIR irradiation, the corrosion resistance can be substantially improved and the repaired coating can still play a long-lasting role as physical barrier to avoid suffering deteriorative corrosion process. Applying noninvasive stimuli of NIR can not only help heal the scratch area and strengthen the corrosion resistance in the repaired region with high-level restoration, but can also serve as a convenient mean to motivate repeatable selfhealing behavior, assisting to protect Mg alloy from fast corrosion started by cracks or defects and to control the degradation rate to a lower speed. The method of photo-controllable degradation in this work provides a novel surface modification for magnesium alloys to meet wide-range application.

Data availability

The raw data required to reproduce these findings are available to download from https://pan.baidu.com/s/1oA9Ts-xrDH9 GmQtXay0Pw].

Declaration of Competing Interest

We declare that all authors have no conflict of interest.

Acknowledgements

This work is jointly supported by the Natural Science Fund of Hubei Province, 2018CFA064, National Natural Science Foundation of China, Nos. 51671081, 51871162, 51801056 and 51422102, and the National Key R&D Program of China No. 2016YFC1100600 (sub-project 2016YFC1100604).

Appendix A. Supplementary data

Supplementary material related to this article can be found, in the online version, at doi:https://doi.org/10.1016/j.corsci.2019.108257.

References

- [1] X. Li, Z.Y. Weng, W. Yuan, X.Z. Luo, H.M. Wong, X.M. Liu, S.L. Wu, K.W.K. Yeung, Y.F. Zheng, P.K. Chu, Corrosion resistance of dicalcium phosphate dihydrate/poly (lactic-co-glycolic acid) hybrid coating on AZ31 magnesium alloy, Corros. Sci. 102 (2016) 209–221
- [2] X. Li, X.M. Liu, S.L. Wu, K.W.K. Yeung, Y.F. Zheng, P.K. Chu, Design of magnesium alloys with controllable degradation for biomedical implants: from bulk to surface, Acta Biomater. 45 (2016) 2–30.
- [3] Y.C. Wang, B.Y. Liu, X.A. Zhao, X.H. Zhang, Y.C. Miao, N. Yang, B. Yang, L.Q. Zhang, W.J. Kuang, J. Li, E. Ma, Z.W. Shan, Turning a native or corroded Mg alloy surface into an anti-corrosion coating in excited CO₂, Nat. Commun. 9 (2018) 4058
- [4] L.Y. Li, L.Y. Cui, R.C. Zeng, S.Q. Li, X.B. Chen, Y.F. Zheng, M.B. Kannan, Advances in functionalized polymer coatings on biodegradable magnesium alloys - a review, Acta Biomater. 79 (2018) 23–36.

[5] Q.Y. Yang, W. Yuan, X.M. Liu, Y.F. Zheng, Z.D. Cui, X.J. Yang, H.B. Pan, S.L. Wu, Atomic layer deposited ZrO₂ nanofilm on Mg-Sr alloy for enhanced corrosion resistance and biocompatibility, Acta Biomater. 58 (2017) 515–526.

- [6] X.M. Liu, Q.Y. Yang, Z.Y. Li, W. Yuan, Y.F. Zheng, Z.D. Cui, X.J. Yang, K.W.K. Yeung, S.L. Wu, A combined coating strategy based on atomic layer deposition for enhancement of corrosion resistance of AZ31 magnesium alloy, Appl. Surf. Sci. 434 (2018) 1101–1111.
- [7] W.H. Fan, Y. Jin, Y.H. Huang, J.Z. Pan, W.N. Du, Z.Y. Pu, Room-temperature self-healing and reprocessing of diselenide-containing waterborne polyurethanes under visible light, J. Appl. Polym. Sci. 136 (2019) 47071.
- [8] Z.Y. Li, G. Davidson-Rozenfeld, M. Vázquez-González, M. Fadeev, J.J. Zhang, H. Tian, I. Willner, Multi-triggered supramolecular DNA/bipyridinium dithienylethene hydrogels driven by light, redox and chemical stimuli for shape-memory and self-healing applications, J. Am. Chem. Soc. 140 (2018) 17691–17701.
- [9] Y.L. Fang, J.C. Li, X.S. Du, Z.L. Du, X. Cheng, H.B. Wang, Thermal- and mechanical-responsive polyurethane elastomers with self-healing, mechanical-reinforced, and thermal-stable capabilities, Polymer 158 (2018) 166–175.
- [10] Z.H. Xie, D. Li, Z. Skeete, A. Sharma, C.J. Zhong, Nanocontainer-enhanced self-healing for corrosion-resistant Ni coating on Mg alloy, ACS Appl. Mater. Interface 9 (2017) 36247–36260.
- [11] C. Ellingford, R.N. Zhang, A. Wemyss, C.R. Bowen, T. McNally, L. Figiel, C.Y. Wan, Intrinsic tuning of poly (styrene-butadiene-styrene)-based self-healing dielectric elastomer actuators with enhanced electromechanical properties, ACS Appl, Mater. Interface 10 (2018) 38438–38448.
- [12] J.Y. Ren, H.Y. Xuan, W. Dai, Y.X. Zhu, L.Q. Ge, Double network self-healing film based on metal chelation and schiff-base interaction and its biological activities, Appl. Surf. Sci. 448 (2018) 609–617.
- [13] J.Y. Chen, X.B. Chen, J.L. Li, B. Tang, N. Birbilis, X.G. Wang, Electrosprayed PLGA smart containers for active anti-corrosion coating on magnesium alloy AMlite, J. Mater. Chem. A Mater. Energy Sustain. 2 (2014) 5738–5743.
- [14] J.E. Gray, B. Luan, Protective coatings on magnesium and its alloys a critical review, J. Alloys. Compd. 336 (2002) 88–113.
- [15] C.D. Ding, J.H. Xu, L. Tong, G.C. Gong, W. Jiang, J.J. Fu, Design and fabrication of a novel stimulus-feedback anticorrosion coating featured by rapid self-healing functionality for protection of magnesium alloy, ACS Appl. Mater. Interface 9 (2017) 21034–21047.
- [16] C.B. Liu, H.C. Zhao, P.M. Hou, B. Qian, X. Wang, C.Y. Guo, L.P. Wang, Efficient graphene/cyclodextrin based nanocontainer: synthesis and host-guest inclusion for self-healing anticorrosion application, ACS Appl. Mater. Interface 10 (2018) 36229–36239.
- [17] E.V. Skorb, A.G. Skirtach, D.V. Sviridov, D.G. Shchukin, H. Möhwald, Laser-controllable coatings for corrosion protection, ACS Nano 3 (2009) 1753–1760.
- [18] J.J. Fu, T. Chen, M.D. Wang, N.W. Yang, S.N. Li, Y. Wang, X.D. Liu, Acid and alkaline dual stimuli-responsive mechanized hollow mesoporous silica nanoparticles as smart nanocontainers for intelligent anticorrosion coatings, ACS Nano 7 (2013) 11397–11408.
- [19] J.P. Wang, J.K. Wang, Q. Zhou, Z. Li, Y.S. Han, Y. Song, S. Yang, X.K. Song, T. Qi, H. Möhwald, D. Shchukin, G.L. Li, Adaptive polymeric coatings with self-reporting and self-healing dual functions from porous core-shell nanostructures, Macromol. Mater. Eng. 303 (2018) 1700616.
- [20] C.D. Ding, Y. Liu, M.D. Wang, T. Wang, J.J. Fu, Self-healing, superhydrophobic coating based on mechanized silica nanoparticles for reliable protection of magnesium Alloy, J. Mater. Chem. A Mater. Energy Sustain. 4 (2016) 8041–8052.
- [21] M.C. Wu, Y. Li, N. An, J.Q. Sun, Applied voltage and near-infrared light enable healing of superhydrophobicity loss caused by severe scratches in conductive superhydrophobic films, Adv. Funct. Mater. 26 (2016) 6777–6784.
- [22] F. Gao, J.C. Cao, Q.B. Wang, R. Liu, S.W. Zhang, J.C. Liu, X.Y. Liu, Properties of UV-cured self-healing coatings prepared with PCDL-based polyurethane containing multiple H-bonds, Prog. Org. Coat. 113 (2017) 160–167.
- [23] G. Ugur, J.Y. Chang, S.H. Xiang, L.W. Lin, J. Lu, A near-infrared mechano responsive polymer system, Adv. Mater. 24 (2012) 2685–2690.
- [24] X.Y. Zou, Y.L. Lin, B. Xu, T.C. Cao, Y.L. Tang, Y. Pan, Z.C. Gao, N.Y. Gao, Enhanced inactivation of *E. Coli* by pulsed UV-LED irradiation during water disinfection, Sci. Total Environ. 650 (2019) 210–215.
- [25] L. Tan, J. Li, X.M. Liu, Z.D. Cui, X.J. Yang, S.L. Zhu, Z.Y. Li, X.B. Yuan, Y.F. Zheng, K.W.K. Yeung, H.B. Pan, X.B. Wang, S.L. Wu, Rapid biofilm eradication on bone implants using red phosphorus and near-infrared light, Adv. Mater. 30 (2018) 1801808.
- [26] Y.I. Ko, Y.J. Lee, K. Devarayan, B.S. Kim, T. Hayashi, I.S. Kim, Annealing effects on mechanical properties and shape memory behaviors of silicone-coated elastomeric polycaprolactone nanofiber filaments, Mater. Lett. 131 (2014) 128–131.
- [27] J. Yang, S.D. Zhai, H. Qin, H. Yan, D. Xing, X.L. Hu, NIR-controlled morphology transformation and pulsatile drug delivery based on multifunctional phototheranostic nanoparticles for photoacoustic imaging-guided photothermal-

- chemotherapy, Biomaterials 176 (2018) 1-12.
- [28] H. Lee, H. Kim, T.P. Nguyen, J.H. Chang, S.Y. Kim, H. Kim, E. Kang, Nanocomposites of molybdenum disulfide/methoxy polyethylene glycol-co-polypyrrole for amplified photoacoustic signal, ACS Appl. Mater. Interface 8 (2016) 29213–29219.
- [29] J. Yuan, J.L. Liu, Q. Song, D. Wang, W.S. Xie, H. Yan, J.F. Zhou, Y. Wei, X.D. Sun, L.Y. Zhao, Photoinduced mild hyperthermia and synergistic chemotherapy by onepot-synthesized docetaxel-loaded poly(lactic-co-glycolic acid)/ polypyrrole nanocomposites, ACS Appl. Mater. Interface 8 (2016) 24445–24454.
- [30] T.F. da Conceicao, N. Scharnagl, C. Blawert, W. Dietzel, K.U. Kainer, Surface modification of magnesium alloy AZ31 by hydrofluoric acid treatment and its effect on the corrosion behaviour, Thin Solid Films 518 (2010) 5209–5218.
- [31] J.H. Kim, A. Mirzaei, H.W. Kim, S.S. Kim, Facile fabrication of superhydrophobic surfaces from austenitic stainless steel (AISI 304) by chemical etching, Appl. Surf. Sci. 439 (2018) 598–604.
- [32] E. Lizundia, T.D. Nguyen, J.L. Vilas, W.Y. Hamad, M.J. MacLachlan, Chiroptical, morphological and conducting properties of chiral nematic mesoporous cellulose/ polypyrrole composite films, J. Mater. Chem. A Mater. Energy Sustain. 5 (2017) 19184-19104
- [33] W.L. Chiang, T.T. Lin, R. Sureshbabu, W.T. Chia, H.C. Hsiao, H.Y. Liu, C.M. Yang, H.W. Sung, A rapid drug release system with a NIR light-activated molecular switch for dual-modality photothermal/antibiotic treatments of subcutaneous abscesses, J. Control. Release 199 (2015) 53–62.
- [34] M. Ascencioa, M. Pekguleryuz, S. Omanovic, Corrosion behaviour of polypyrrole-coated WE43 Mg alloy in a modified simulated body fluid solution, Corros. Sci. 133 (2018) 261–275.
- [35] P. Xiang, S.S. Wang, M. He, Y.H. Han, Z.H. Zhou, D.L. Chen, M. Li, L.Q. Ma, The in vitro and in vivo biocompatibility evaluation of electrospun spider silk protein/PCL/ gelatin for small caliber vascular tissue engineering scaffolds, Colloids Surf. B Biointerfaces 163 (2018) 19–28.
- [36] J. Vega, H. Scheerer, G. Andersohn, M. Oechsner, Experimental studies of the effect of Ti interlayers on the corrosion resistance of TiN PVD coatings by using electrochemical methods, Corros. Sci. 133 (2018) 240–250.
- [37] A. Ghafari, M. Yousefpour, A. Shanaghi, Corrosion protection determine of ZrO₂/AA7057 nanocomposite coating with inhibitor using a mathematical ranking methods, Appl. Surf. Sci. 465 (2019) 427–439.
- [38] C.O. Hoog, N. Birbilis, Y. Estrin, Corrosion of pure Mg as a function of grain size and processing route, Adv. Eng. Mater. 10 (2008) 579–582.
- [39] D. Song, A.B. Ma, J.H. Jiang, P.H. Lin, D.H. Yang, J.F. Fan, Corrosion behaviour of bulk ultra-fine grained AZ91D magnesium alloy fabricated by equal-channel angular pressing, Corros. Sci. 53 (2011) 362–373.
- [40] L.C. Córdoba, M.F. Montemor, T. Coradin, Silane/TiO₂ coating to control the corrosion rate of magnesium alloys in simulated body fluid, Corros. Sci. 104 (2016) 152–161.
- [41] M. Sun, A. Yerokhin, M.Y. Bychkova, D.V. Shtansky, E.A. Levashov, A. Matthews, Self-healing plasma electrolytic oxidation coatings doped with benzotriazole loaded halloysite nanotubes on AM50 magnesium alloy, Corros. Sci. 111 (2016) 753–769.
- [42] C.D. Ding, Y. Tai, D. Wang, L.H. Tan, J.J. Fu, Superhydrophobic composite coating with active corrosion resistance for AZ31B magnesium alloy protection, Chem. Eng. J. 357 (2019) 518–532.
- [43] D. Snihirova, L. Liphardt, G. Grundmeier, F. Montemor, Electrochemical study of the corrosion inhibition ability of "smart" coatings applied on AA2024, J. Solid State Electrochem. 17 (2013) 2183–2192.
- [44] C.M. Wang, J. Shen, F.X. Xie, B. Duan, X. Xie, A versatile dopamine-induced intermediate layer for polyether imides (PEI) deposition on magnesium to render robust and high inhibition performance, Corros. Sci. 122 (2017) 32–40.
- [45] J. Jayaraj, S.A. Raj, A. Srinivasan, S. Ananthakumar, U.T.S. Pillai, N.G.K. Dhaipule, U.K. Mudali, Composite magnesium phosphate coatings for improved corrosion resistance of magnesium AZ31 alloy, Corros. Sci. 113 (2016) 104–105.
- [46] G.L. Song, Z. Shi, Corrosion mechanism and evaluation of anodized magnesium alloys, Corros. Sci. 85 (2014) 126–140.
- [47] H. Gao, Q. Li, F.N. Chen, Y. Dai, F. Luo, L.Q. Li, Study of the corrosion inhibition effect of sodium silicate on AZ91D magnesium alloy, Corros. Sci. 53 (2011) 1401–1407.
- [48] G. Zhang, L. Wu, A.T. Tang, Y.L. Ma, G.L. Song, D.J. Zheng, B. Jiang, A. Atrens, F.S. Pan, Active corrosion protection by a smart coating based on a MgAl-layered double hydroxide on a cerium-modified plasma electrolytic oxidation coating on Mg alloy AZ31, Corros. Sci. 139 (2018) 370–382.
- [49] P. Xiong, Z.J. Jia, W.H. Zhou, J.L. Yan, P. Wang, W. Yuan, Y.Y. Li, Y. Cheng, Z.P. Guan, Y.F. Zheng, Osteogenic and pH stimuli-responsive self-healing coating on biomedical Mg-1Ca alloy, Acta Biomater. 92 (2019) 336–350.
- [50] M. Yan, V.J. Gelling, B.R. Hinderliter, D. Battocchi, D.E. Tallman, G.P. Bierwagen, SVET method for characterizing anti-corrosion performance of metal-rich coatings, Corros. Sci. 52 (2010) 2636–2642.